Tunable all-solid-state wire-shaped high power device based on carbon nanotubes yarn

Carbon 213 (2023) 118283

Contents lists available at ScienceDirect

Carbon

journal homepage: www.elsevier.com/locate/carbon

Tunable all-solid-state wire-shaped high power device based on carbon nanotubes yarn

Mara Serrapede [a,b,1,*], Francesco Seller [a,b,1], Pietro Zaccagnini [a,b], Micaela Castellino [a], Ignazio Roppolo [a,b], Felice Catania [a], Jennifer Tata [c], Tiziano Serra [c], Stefano Bianco [a], Andrea Lamberti [a,b]

[a] Politecnico di Torino, Dipartimento di Scienza Applicata e Tecnologia (DISAT), Corso Duca Degli Abruzzi, 24, 10129, Turin, Italy
[b] Istituto Italiano di Tecnologia, Center for Sustainable Future Technologies, Via Livorno 60, 10144, Turin, Italy
[c] MARTUR Italy Srl, Via Stefano Scoffone 3, 10095, Grugliasco, Italy

A B S T R A C T

Energy storage devices integrated into textiles have emerged as a significant strategy for electronic applications. In this context, in the present paper novel flexible devices were developed, in which the control of both the electrode characteristics and the solid-electrolyte properties allows to build all-solid-state wire-shaped supercapacitors that can be integrated and waved. The proposed device was assembled using modified CNT yarns as electrodes and a blend of ionic liquid, Li salt and poly(ethylene glycol) acrylate to fabricate the solid-polymeric electrolyte. Excellent performance in terms of both electrochemical parameters and stability were obtained. These achievements are possible thanks to the coupling of asymmetric CNT yarns, following an optimization of the activation procedure together with the improvement of the polymeric electrolyte. The results show a capacitance as high as 1.8 mF/cm, energy density of 1.3 μWh/cm and a capacitance retention higher than 100% over 1200 cycles.

1. Introduction

In the last few decades, together with the tremendous growth of portable electronics, the miniaturization of integrated circuits has proceeded at an exponential rate. However, the miniaturization of power sources did not follow the same trend, and hence the size of a fully integrated power device is now the limiting factor to design completely autonomous micromachines [1]. Wire-shaped architectures emerged a decade ago as one of the most promising strategies to increase the integration level, especially into textiles [2,3]. The key challenges are the choice and the design of bendable electrodes and current collectors, with improved mechanical properties, as well as the fabrication of flexible electrolytes with high ion conductivity and the optimization of packaging, to assure a perfect sealing of the whole device.

As one type of micro-electrochemical energy storage device, wire-shaped supercapacitors offer much larger power densities when compared to conventional batteries and supercapacitors, due to the short ion diffusion path arising from the thin film of the electrolyte [4]. To overcome the limitation of specific capacitance related to the small diameter of conductive wires, the majority of research articles reports composite electrodes in which the current collectors (metallic, or polymeric filled with CNT or carbon fibres) are decorated with either carbon structures to improve the EDLC (electrical double layer capacitance) or with organic/inorganic additives to increase the pseudo-capacitance. The main drawback of such a strategy consists in the low power density of the overall device and on the low mechanical stability. In summary, the achievement of high capacitance, fast electrical transport, high mechanical stability and good rate capability depends on the rational design of electrodes.

Most of the works in the field of portable and wearable supercapacitors are focused on the surface modification of light-weight electrodes [5] and on the study of solid state electrochemistry, in which high ion-conducting materials are developed for storage applications and energy conversion [6–8]. Differently, here we propose for the first time a wire-shaped supercapacitor with electrochemically activated commercial carbon nanotube yarns (yCNT) together with a solid-state electrolyte that can solve the above-mentioned issues. The electrochemical activation of the yCNT allowed an increase in the amount of defect sites and heterogeneous atoms at the electrodes [9,10] resulting in a homogeneous corrosion of the originally highly ordered surface. By controlling the electrochemical activation conditions in a concentrated acid solution, an enormous increase of the capacitance was

* Corresponding author. Politecnico di Torino, Dipartimento di Scienza Applicata e Tecnologia (DISAT), Corso Duca Degli Abruzzi, 24, 10129, Turin, Italy.
E-mail address: mara.serrapede@polito.it (M. Serrapede).
[1] These authors equally contribute to the work.

https://doi.org/10.1016/j.carbon.2023.118283
Received 5 May 2023; Received in revised form 19 June 2023; Accepted 5 July 2023
Available online 5 July 2023

achieved while maintaining the yCNT network.

Polymer electrolytes have been proved to be promising materials for electrochemical devices to achieve good electrochemical stability and conductivity. Regarding safety issues and processability, solid polymer electrolytes (SPEs) offer great advantages over liquid electrolytes in energy storage devices, overcoming several issues such as electrolyte leakage and internal short circuits and reducing the possibility of electrolyte combustion in case of external fire. Nevertheless, the main disadvantage of a SPE is the reduction of the ionic conductivity when compared with polymers that hold even a small fraction of liquid electrolytes, although the reduction of the film thicknesses can increase the real conductance of the full cell. Polyether electrolytes are of considerable scientific interest since 1973 when Fenton, Parker and Wright discovered the ionic conductivity in complexes of alkali metal salts with PEO (Polyethylene oxide) [11] and a few years later they were employed as separators in Li-metal batteries [12]. The ionic conductivity in this type of polymer electrolyte requires local relaxation and segmental motion of the solid solvent (PEO) chains to allow fast ion transport, while the low ionic conductivity (10^{-8} to 10^{-4} S cm^{-1}) of the complexes is attributed to the high degree of crystallinity of the polymer itself, so that the ionic conduction mostly occurs within the amorphous regions of the polymeric matrix [13]. The conductivities at room temperature and below are often not sufficient for their use in applications where high rates are required except if considering the relatively high temperature of operation (80–100 °C), where the conductivity is of the order of 10^{-3} S cm^{-1}, due to better solvation of the Li salt in the polymer matrix and a faster polymer motion. Therefore, at elevated temperatures SPEs are superior to liquid electrolytes in terms of safety, stability and aging [14,15]. The transport properties of crystalline and amorphous polymer electrolytes are therefore still of very great active interest.

Solid polymer electrolytes based on the polymerization of poly (ethylene glycol) diacrylate (PEGDA) and poly(propylene glycol) diacrylate (PPGDA) are considered as interesting alternative materials. The polymerization of a polyacrylates [16,17] with a highly cross-linked network could facilitate the ionic conduction either when employed as a gel swelled with liquid electrolyte or as a dry polymer electrolyte in which the ionic conduction is achieved through the coordination of cations to the oxygen atoms in the chains so that the polymer acts as a solid solvent. In this project, PEGDA was copolymerized with a monofunctional poly(ethylene glycol) methyl ether acrylate (PEGMEA), in order to increase the segmental motion of the chains and the flexibility of the polymeric matrix. The addition of bis(trifluoromethanesulfonyl) imide salts ($TFSI^+$), prior to the polymerization, allowed to employ the copolymer as a good electrolyte and the bulky TFSI anions promoted even greater flexibility and stretchability due to their plasticization effect [18]. The most conductive and mechanically stable solid polymer polyelectrolyte among those studied was then UV cured onto the yCNT electrodes to prepare a thin and conformal coating with good ionic conductivity and mechanical strength which serves both as separator and electrolyte in a wire-shaped supercapacitor.

Here, the activation degree of the electrodes was deeply characterized by means of Raman spectroscopy, X-ray Photoelectron Spectroscopy (XPS) and cyclic voltammetry (CV). The ionic conductivity of the polymerized films was measured by Electrochemical Impedance Spectroscopy (EIS) and the homogeneity was observed at the Field Emission Scanning Electron Microscope (FESEM). The degree of polymerization was observed by means of Infrared Spectroscopy (FTIR) and X-Ray Diffractomery (XRD). To correlate the ionic conductivity with the ion mobility, Dynamic Mechanical Analysis (DMA) was performed. Symmetric and asymmetric devices were obtained by joining two 150-μm diameter yCNTs (symmetric) and one activated-yCNT as the negative electrode and two twisted yCNTs as the positive electrode (asymmetric) in an all-solid-state polyionic polymer electrolyte. The devices show a voltage up to 1.7 V and 2.3 V, respectively, with a maximum capacitance of 1.42 and 1.85 mF/cm respectively measured at 1 mV/s. Even if the device is bent the capacitance retention is well maintained.

2. Experimental

2.1. Materials

Carbon nanotube yarns (yCNT) of 130, 150 and 600 μm in diameter were purchased by DMAX. Different diameters were employed for different purposes and to balance the capacitances. Potassium hydroxide (KOH), nitric acid (HNO_4), and sulfuric acid (H_2SO_4) were used to activate the yCNT. The formulation for the solid-state polyelectrolyte is based on poly(ethylene glycol) diacrylate (PEGDA, Mn ≈ 575) macromonomer, monofunctional poly(ethylene glycol) methyl ether acrylate (PEGMEA, Mn ≈ 480), lithium bis(trifluoromethanesulfonyl)imide (Li TFSI battery grade dried overnight in a vacuum oven at 120 °C) were purchased from Merck-Sigma Aldrich and 1-Ethyl-3-methylimidazolium bis(trifluoromethylsulfonyl)imide (EMIM TFSI, electronic grade) was purchased from Solvionic. 2-Hydroxy-2-methylpropiophenone from Shandong Chuangying Chemical was employed as the photoinitiator. All the work on solid polymer electrolytes was carried out in a glove box.

2.2. Electrodes preparation and polymerization of the PEGDA-PEGMEA solid polyelectrolyte

Prior to any electrochemical activation, the yCNTs were immersed in 1 M KOH for 2 h at 60 °C to increase the wettability of the surface. They were then rinsed with distilled water to remove any salt residual. The activation of yCNT was carried out in a cell consisting of three electrodes where the yCNT, a platinum bar and an Ag/AgCl 3 M KCl acted as working, counter and reference electrodes, respectively. After the immersion in KOH solution, the working electrode was activated by dynamic cycling in 4 M HNO_3 at 10 mV/s from open circuit potential (OCP) towards more positive values. By changing the upper limit from 1.74 V to 1.84 V and the number of cycles, a different degree of activation was obtained. To monitor the degree of activation, cyclic voltammograms were carried out in 0.5 M H_2SO_4. The activation was then confirmed by Raman spectroscopy and a quantification of the functional groups was carried out by XPS.

The preparation of the polyelectrolyte solid network did not involve any solvent, nor a time-consuming procedure. Li TFSI salt and EMIM TFSI were stirred in equal amounts (in weight) at 70 °C until the full dissolution of the salt was achieved [19]. Mixtures of PEGDA and PEGMEA were prepared at room temperature by varying their mass fraction and, when homogeneous, the salt solution was added by mechanical stirring. In all the tested mixtures, the 80 wt% of the total weight belonged to the polyionic salts. The proportion of the remaining 20% of the polymeric network was investigated as 20 wt% PEGDA and 0 wt% PEGMEA, 15 wt% PEGDA and 5 wt% PEGMEA, 10 wt% PEGDA and 10 wt% PEGMEA and 5 wt% PEGDA and 15 wt% PEGMEA. The PEGMEA to PEGDA ratio in the polymeric network was therefore varied from 0 to 3 by weight while fixing an equal amount of salts which also act as plasticizers (40% each salt of LiTFSI and EMIMTFSI), so that the samples become *a*PEGDA *(20-a)*PEGMEA 40EMIMTFSI 40LiTFSI with $20 < a < 5$ by weight. The whole article *a*, therefore, refers to the % of PEGDA. A further decrease in PEGDA concentration led to a not-solid network, while the amount of the chosen salts ensured the highest flexibility of the solid matrix, among those tested. For these two reasons, the physical-chemical characterization is presented only for the cited samples. In all the tested formulations, the photoinitiator was added at a concentration of 2 wt% of the photo-curable monomers. Prior to UV-curing, the blends were cast onto aluminum foil or directly onto the electrodes. It is worth noticing that the blends have low viscosity. UV-curing followed two steps: first using a UV-lamp (Hamamatsu LC 8) equipped with an optical fiber (light intensity 20 mW cm^{-2}) for 2 min, then the semi-solid electrolyte was irradiated with a high-pressure UV-lamp (Robofactory UV curing box, light intensity 5 mW cm^{-2} for 5 min). The first step of polymerization was essential to freeze the thickness of the electrolyte and to get reproducible and uniform

thicknesses (500 ± 10 μm). The solid films were easily peeled off from the substrate and used for the characterizations after dehydration at 80 °C overnight.

2.3. Characterization of materials

The activation and characterization of yCNT electrodes was performed by using a potentiostat/galvanostat Biologic VMP3 by means of cyclic voltammetry in 4 M HNO_3 and 0.5 M H_2SO_4, respectively. The latter was employed to compare the activations of this study with those of Zhu et al. [9]. The experiments were carried out in a three-electrode cell in which a platinum bar and an Ag/AgCl 3 M KCl counter and reference electrodes were used under nitrogen gas.

X-ray photoelectron spectroscopy (XPS) measurements were performed with a Physical Electronics system (PHI 5000 Versa Probe), equipped with monochromatic X-ray Al Kα (1486.6 eV energy) source and a combined e^- and Ar^+ system for charge compensation. The calibration of the binding energy scale was obtained by assigning an energy value of 284.5 eV to the main contribution (C–C) of the C 1s region. Background subtraction in high-resolution scans was performed by means of a Shirley function. Data analysis was carried out with Casa XPS software. XPS spectra were acquired on activated yCNT at different activation times (number of cycles) in order to quantify the functional groups induced by the activation procedures.

Raman spectra were collected by using Renishaw InVia Reflex micro-Raman spectrometer (Renishaw plc, Wottonunder-Edge, UK), equipped with a cooled CCD camera, with a laser excitation wavelength of 514.5 nm and a laser spot size of 10 μm to verify the effect of the activation surface treatment yCNTs.

Fourier transform infrared (FTIR) spectra were recorded by using a Nicolet 5700 FTIR spectrometer equipped with an attenuated total reflectance (ATR) with 2 cm^{-1} resolutions and an average of 32 scans. The assignments of the peaks in the ATR spectra were made according to previous studies [20–23].

Dynamic mechanical Analysis (DMA) was employed to measure the viscoelastic properties of the materials. Testing was performed using a Triton Technology TTDMA equipment, and the measurements were carried out from −80 to 20 °C, with a heating rate of 3 °C min^{-1} in tensile configuration (frequency 1 Hz, strain 20 μm). Glass transition temperature (T_g) was determined as the maximum of $tan\delta$ curve (where δ is the phase lag between stress and strain).

The ionic conductivity of the solid polyionic electrolytes was estimated using Biologic VMP300 equipped with AC impedance modulus at AC V_{rms} = 10 mV and 0 V vs. OCP dc bias within a frequency range of 1 MHz and 1 Hz. The samples were previously cast, as described in the Experimental section, then disks of 15 mm in diameter were cut and measured inside a EL-cell in between two stainless steel spacers between 25 and 125 °C. The activation energy was calculated based on the Arrhenius and Vogel–Fulcher–Tammann models.

The morphological characterization was carried out by means of a Field-Emission Scanning Electron Microscope (FESEM Supra 40, manufactured by Zeiss), equipped with an Oxford instruments EDX Si(Li) detector (10 mm^2 detection area). The images containing morphological information were acquired by the InLens detector with a 45° tilted sample holder.

The determination of the potential window of the yCNT and the activated-yCNT was carried out in a homemade thee electrode cell setup, in which the most conductive solid polyionic electrolyte was placed between a yCNT, an activated carbon coated electrode and a titanium gauge, as working, counter and pseudo-reference electrodes, respectively. The electrochemical cells were vacuum-sealed in coffee bags in order to prevent any gas and moisture interfering with the experiments. Devices were characterized with the Biologic apparatus by cyclic voltammetry, with incremental maximum voltage to find the operating voltage according to a coulombic efficiency above 98% at 1 mV/s, and increasing rates up to 1 V/s to evaluate the rate capabilities and the energy and power densities of such devices. Float tests at the maximum operating voltage were carried out for 24 h and the self-discharge was monitored over 24 h.

3. Results and discussion

3.1. Wire shaped CNT yarn as electrodes

The activation of the commercial yCNT was carried out in 4 M HNO_3 by means of cyclic voltammetry scanning from −0.06 V to 1.84, 1.89 and 1.94 V vs. Ag/AgCl. During the cathodic scans, the peak at 550 mV moved progressively more positively to reach, at the 4th cycle, 650 mV, but at the same time, the rate (current) associated with this process decreased (as shown in Fig. 1a). As this peak is closer to the onset potential of the oxidation process at 1.23 V (for all mentioned cycles), an increase in the reduction kinetics is observed for the first 4 voltammetries of activation. In contrast, by increasing the number of cycles the current density of this reduction peak became smaller, the potential moved further from the oxidation onset potential and the capacitance of the electrode decreased massively (Fig. 1 b top) indicating both a decrease in the electronic conductivity of the electrode and a worsening in the kinetics of the process. The same trend was observed when the positive potential was moved from 1.84 V to more positive values: already at the second scan it is possible to observe an increase in the electronic resistivity of the electrode (Fig. 1 b bottom). Lower positive potentials were tested and the data are not shown since the voltammetry did not show evidence of the activation reactions. For those reasons, the activation of yCNT electrodes in this study was performed under the conditions of a maximum potential of 1.84 V, four activation cycles with 10 mV/s of scan rate. It is worth mentioning that the higher the resistive response in the voltammetric cycles, the lower the mechanical properties of the activated yCNT: in the harsher activation condition (at the 10th cycle with a maximum positive potential of 1.94 V) the yCNT completely corroded and broke down at the solution meniscus. Therefore, the worsening of the electrical conductivity can be linked to physical damage to the electrode, which compromises the electrical conduction.

As shown in Fig. 1 c, the changes in the well-ordered structure of the yCNT upon activation were analysed by Raman spectroscopy. Three peaks appear in the Raman spectra of the samples: the D-band at ~1350 cm^{-1} (related to the defectiveness in the graphitic plane), the G-band at ~1580 cm^{-1} (related to planar vibrations in sp^2 hybridized carbons) and 2D-band at ~2700 cm^{-1} (the overtone of the D-band, related with the long-range order of the graphitic structure) [24,25]. At the fourth activation cycle, the intensity of the 2D-band decreased and the ratio between the D and G peaks increased (from 0.017 to 0.270), giving evidence that the activation promotes an increase in the number of defects in the graphitic domains [26].

XPS analysis was performed on samples subjected to 1st to 4th cycles. This analysis was used to determine the relative atomic concentration (at. %) of each element present on sample surfaces (as reported in Table 1), calculated from HR spectra. The more intense peaks have been assigned to C1s and O1s, while some traces have been attributed to N1s, S2p and Ca2p, which are due to chemical treatments remnants or environmental contamination. From the data, a clear trend in the O peak evolution due to activation processes was observed, reaching the highest intensity in the 4th cycle sample (17.4 at. %) starting from 13.0 at. % for the 1st cycle sample. C1s core level peak was analysed to establish the relative amount of graphitic species, together with the bonds related to oxygen species. To perform the deconvolution procedure of the C1s peak, the extensive work done by M. Smith et al. [27], was taken as reference. In this study, the authors reported a detailed study, from both experimental and theoretical (by means of DFT – Density Functional Theory calculations) points of view, on disordered oxygenated C-based materials. Apart from the well-known chemical shifts due to C–C sp^2 (at 284.5 eV), two other C–C bonds related to “defect sites” in a graphitic

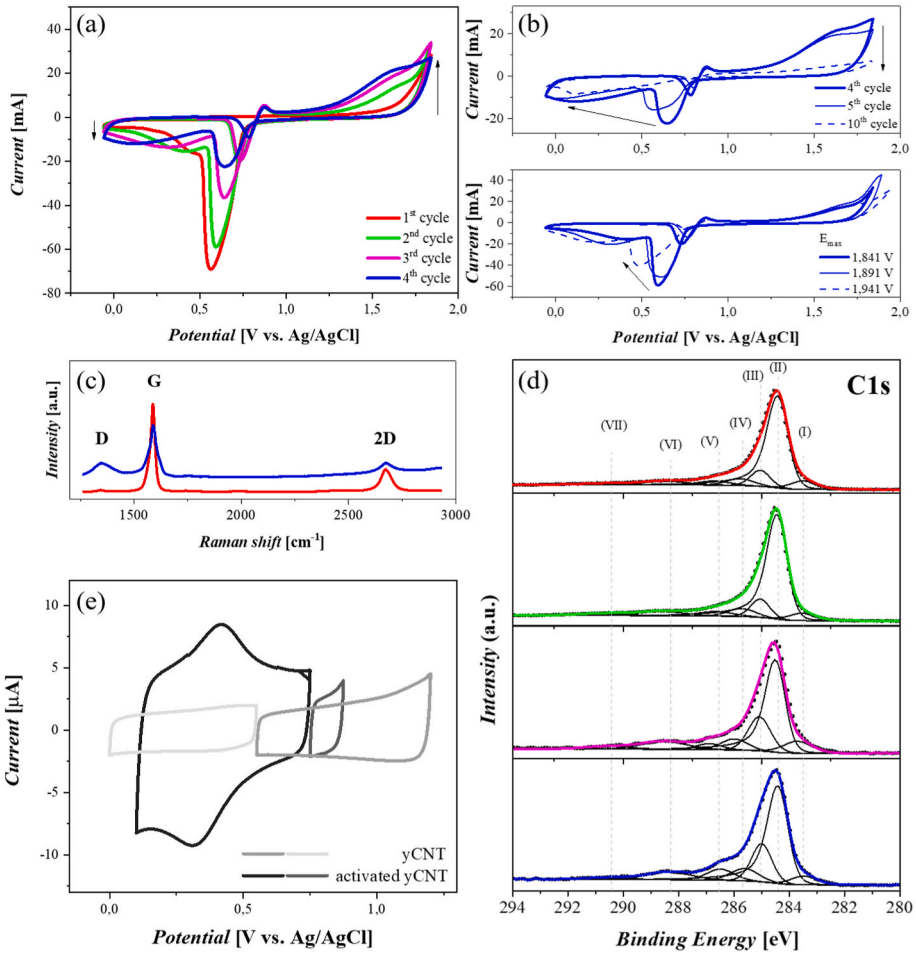

Fig. 1. (a) First four voltammograms of the activated yCNT in 4 M HNO_3 at 10 mV/s, (b.top) voltammograms at the cycle 4th, 5th and 10th, (b.bottom) 2nd voltammogram of activated yCNT at 1.84, 1.89 and 1.94 V. (c) Raman. (d) XPS HR C1s spectra with deconvolution curves for samples at 1st, 2nd, 3rd and 4th cycles (e) and (f) Comparison of cyclic voltammograms of yCNT and activated yCNT in 0.5 M H_2SO_4 (600 µm, 4 mV/s).

Table 1
XPS relative atomic concentration and C1s core level assignments evaluated from deconvolution procedures (reported in Fig. 1d).

	1st cycle	2nd cycle	3rd cycle	4th cycle
	Relative atomic concentration (at.%)			
C1s	85.2	86.3	81.1	80.1
O1s	13.0	11.8	17.2	17.4
Others	1.8	1.9	1.7	2.5
	Carbon species (%)			
C–C low (peak I)	6.4	5.1	8.0	5.0
C–C sp^2 (peak II)	67.8	67.5	52.3	53.5
C–C high (peak III)	9.3	9.3	17.2	17.4
C–O/C–N (peak IV)	5.7	5.8	7.2	7.7
C–C–O/C═O (peak V)	4.0	4.4	3.8	6.8
O–C═O/COOH (peak VI)	4.9	5.3	8.4	7.7
π−π* (peak VII)	1.9	2.6	3.1	1.9

matrix were introduced: a first one around 283.3–283.8 eV, due to lower coordination, as in the case of sp^1 or Stone-Wales dislocations (*C–C low*) and another around 285.0 eV due to sp^3 allotropes (*C–C high*). Then, all the chemical shifts due to Carbon and Oxygen (or Nitrogen) interaction at 285.6–286.0 eV (C–O/N), 286.5–287.0 eV (O–C–O/C═O), 288.5–289.0 eV (O–C═O) and the shake-up satellite due to π−π* transition at binding energy (BE) > 290 eV were considered. The deconvolution procedures and relative chemical species percentages are shown in Fig. 1 d and Table 1. There is a trend in the reduction of the components related to graphitic carbon C–C sp^2, especially passing from 1st cycle (67.8%) to 4th cycle sample (53.5%), in accordance with the increase of peak III, assigned to C–C defects due to sp^3 species. The latter component increased from 9.3% for the 1st cycle sample to 17.4% for the 4th cycle one, almost doubling. Also, the components related to C–O bonds (peak IV-VI) increase their relative intensity due to activation procedures. So XPS has highlighted that the number of cycles is crucial in modifying the ordered structure of pristine CNT yarns, by introducing more structural defects together with new functionalities due to C–O bonds.

Consistently with Raman and XPS, CV of the activated-yCNT in sulfuric acid also shows modified profiles (used as a comparison with standard literature [10]): the whole potential window shortens and the overall capacitance increases. In particular, the activation induces higher capacities in the cathodic range (+450% on a yCNT of 600 µm of diameter) while the anodic capacities remain almost stable (+18%), as shown in Fig. 1 e. The decrease of the potential widows and the increase in the capacitance both point to the formation of surface groups and to an increase in the roughness or in the disorder which increases the capacitance, as measured by XPS and Raman spectroscopies. The increase in the functionalities allows better compatibility with the hydrophilic nature of the polymeric matrix based on acrylates. The yCNT electrodes were then characterized in the most conductive solid polyionic electrolyte, which also showed good flexibility.

3.2. Solid polyelectrolyte

Ionic conductivity is of paramount importance in the development of

solid polymer electrolytes, since their main function is to provide and to shuttle ions. Moreover, other properties should be considered for specific operations (i.e., the usage in flexible devices or high temperatures), which in turn can strongly modify the ion transport. The characteristics that a polymer matrix should maintain over time are (i) a good solubility for the chosen salts, (ii) a low glass transition temperature T_g, (iii) high electrochemical and mechanical stability towards the used electrodes, (iv) a low degree of crystallinity and (v) low sensitivity towards temperature variations [28]. Here, we employed a PEG-based co-polymer to achieve the aforementioned purposes. The composition of the salts was xLiTFSI and (x-1) EMIMTFSI (x = 0.58) and they were easily mixed together when heated. The two salts were mixed at 70 °C with the monomers in order to melt the crystalline domains of the Li TFSI, which reduce the conductivity, obtaining clear mixtures in all the cases [19]. After photopolymerization, the solid polyionic electrolytes maintained their transparency, indicating good miscibility among all the chemical compounds, and no phase separation was observed. UV light at 20 mW cm^{-2} for 5 min ensured a good degree of polymerization. Longer exposure times did not increase the degree of polymerization and induced a color change in the solid polyionic electrolyte (no colour to yellow) while maintaining high transparency. FT-IR was used to check polymerization and the presence of relevant peaks. In this context, liquid PEGDA, PEGMEA and EMIM TFSI are compared with all the polymerized films. In the spectra (Fig. 2a and Fig. 2b) the typical absorbance bands of EMIM TFSI (blue areas) are evidenced with blue rectangles: in detail the C–SO_2–N bending mode of TFSI (1330 cm^{-1}) and the at 1575 cm^{-1} and 3390 cm^{-1} belong to C–N bending and N–CH_3 stretching of EMIM TFSI respectively are evidenced. Furthermore, at low wavenumbers (around 750 cm^{-1}) it is possible to recognize a series of peaks associated with the C–S and S–N stretching modes [29]. These peaks are visible also in all the samples containing the ionic liquid. Similarly, the peaks relative to PEGDA and PEGMEA are evidenced (orange rectangles). In particular, the CH stretching modes around 2900 cm^{-1} and then the range between 1750 cm^{-1} and 1550 cm^{-1}, which is magnified in Fig. 2 b [30]. In this part, in all the spectra containing PEGDA and PEGMEA it is possible to evidence the presence of a peak at 1720 cm-1 relative to C═O carbonyl group, while the peak relative to C═C acrylic double bonds (at 1640 cm-1 and at 810 cm-1, not shown) completely disappears in the cured samples, indicating successful photopolymerization and complete conversion [31].

In this part, it is possible to evidence the peak at 1720 cm^{-1} relative to C═O carbonyl group while the peak relative to C═C acrylic double

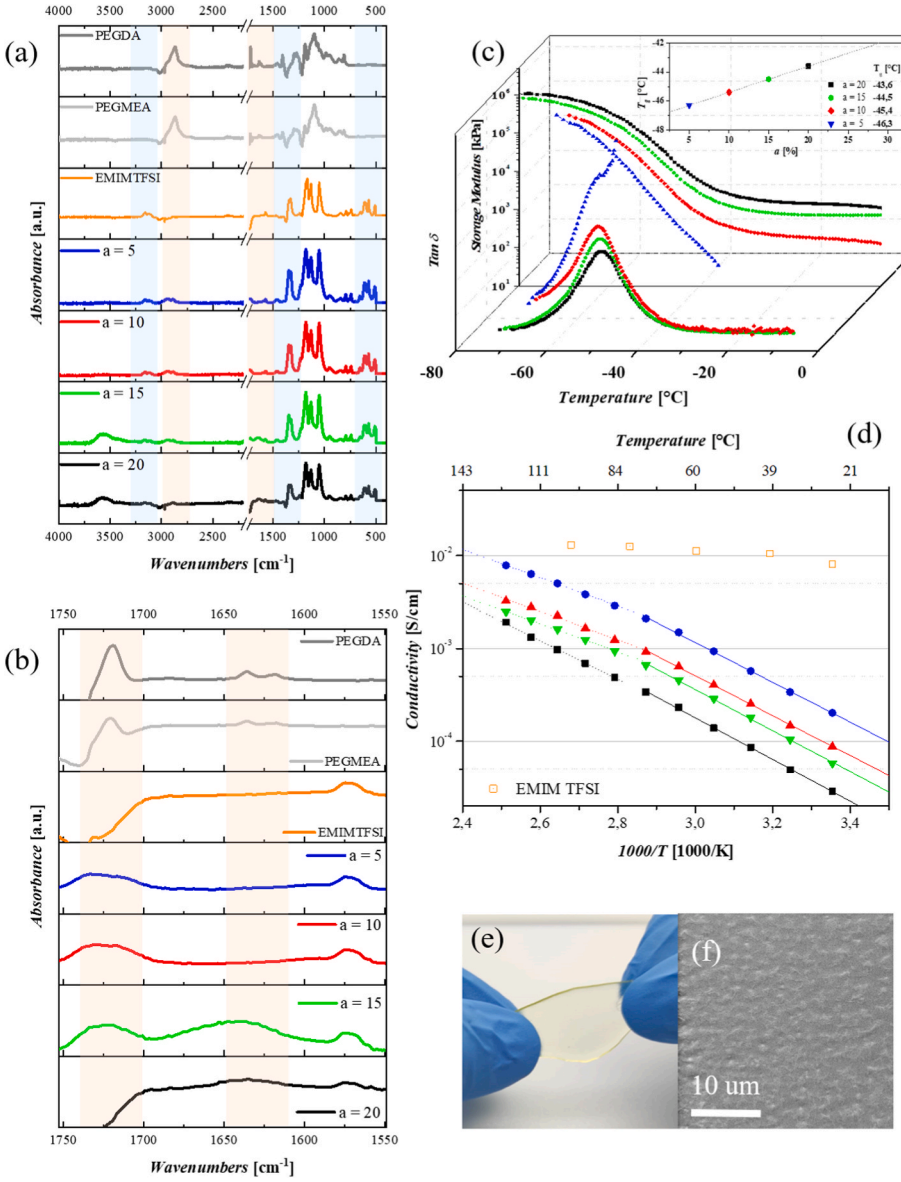

Fig. 2. FTIR spectra of the solid polyionic electrolyte (a) from 4000 to 450 cm^{-1} and (b) zoomed from 1750 to 1550 cm^{-1}. (c) DMA experiment for solid polymer polyelectrolytes at various fractions of PEGDA and PEGMEA: storage modulus and tan(δ) as a function of temperature and (inset) glass transition temperature as a function of PEGDA fraction in the membranes. The red line is the Gordon-Taylor fit to the experimental results. (d) Ionic conductivity obtained different temperatures. The experimental data are reported as dots and the Arrhenius fits are reported as lines. (e) Picture of the solid polyionic electrolyte during stretching tests and (f) FESEM image acquired with InLens detector at 5 kV. (A colour version of this figure can be viewed online.)

bonds (around 1640 cm^{-1}) is present only in the uncured monomers (PEGDA and PEGMEA), while it disappears in the cured samples, indicating successful polymerization. Dynamic mechanical analysis (DMA) experiments were performed to correlate the viscoelastic properties of the membranes with their composition. As expected, on increasing the amount of PEGMEA in the composition, T_g decreases at lower temperatures (Fig. 2 c and Table 2). Furthermore, the storage modulus (E′) in the rubbery region (i.e. above T_g) decreases on increasing the content of PEGMEA. This is an indication of the decrease of crosslinking density, expected to introduce a monofunctional monomer such as PEGMEA [32]. As a consequence, the samples with the highest PEGMEA content did not show a rubbery plateau, but a continuous decrease of E', which suggests that this formulation behaves more as a linear polymer than as a thermoset. The results here shown are in good agreement with previous studies of Fu and Kyu on similar systems [23]. In our samples, there was an additional effect of TFSI salts that act as plasticizers, decreasing both T_g and moduli. Fig. 2 c shows the Gordon-Taylor fit of the estimated glass transition temperatures with respect to the PEGDA concentration.

Electrochemical impedance spectroscopy (EIS) analysis was carried out between 25 °C and 125 °C during the isotherms. The ionic conductivities σ were determined by the bulk resistance R_b, therefore by the real component when the imaginary component equals zero, according to Ref. [1]:

$$\sigma\,(T) = \frac{l}{A \bullet R_b(T)} \qquad [1]$$

where l and A are the thickness and the area of the solid electrolyte, respectively. The ionic conductivity plot for all samples is shown in Fig. 2 d: the graph demonstrates that the conductivity changes and it is highly influenced by varying the co-network compositions while maintaining fixed salt concentrations. The conductivity increases with lowering the PEGDA amount, and a value above 0.1 mS cm^{-1} at room temperature (the lower limit necessary for an electrolyte to work in energy storage) is achieved for all the samples at temperatures above 40 °C. The sample with the highest conductivity (0.2 mS cm^{-1} at 25 °C) is the one in which the monomer was three times higher with respect to the dimer, while it reaches the superionic conductivity at 50 °C [33]. The PEGDA concentration was not further decreased since, with 5% of PEGDA in the electrolyte, the membrane shows flowing, typical of linear polymers. It is worth mentioning that even at this concentration the solid polymer polyelectrolyte retains good elastic and mechanical integrity under stress, as shown in Fig. 2 e. The *log(σ) vs. 1000/T* plot of the samples reveals a curvature and not a pure-Arrhenius trend: usually solid ionic conductors follow two distinct trends with respect to temperature, namely the Arrhenius trend in equation [2] (below T_g) and the Vogel–Fulcher–Tammann trend in equation [3] (above T_g) [34]:

$$Arrhenius\ trend: \sigma\,(T) = \sigma_0 \exp\left(\frac{-E_a}{R \bullet T}\right) \qquad [2]$$

$$Vogel - Fulcher - Tamman\ trend: \sigma\,(T) = \sigma_0 \exp\left(\frac{-E_a}{R \bullet (T - T_0)}\right) \qquad [3]$$

where σ_0 is a pre-factor, T_0 is the ideal glass transition temperature, E_a is the activation energy which is normalized by the gas constant R. The latter approximation usually explains a non-linear transport behavior due to different bond energies and their fluctuations [35]. In this case, either below and above 75 °C, Arrhenius trends fit the experimental data, so in Table 2 we summarize the best-fit parameters obtained from temperature-dependent ionic conductivity plots in Fig. 2 d below 75 °C. In Table 2, the value of σ_0 is related to the overall number of charge carriers, and the lower the PEGDA content, the higher this pre-factor number becomes, suggesting a higher availability of charges free to move in the solid polyelectrolyte. The apparent activation energy E_a can be regarded as the energy barrier for the rotational motion of the polymer segments which decreases by decreasing the PEGDA. Increasing PEGMEA side-chain branches, the ionic transport is enhanced, which may be attributed both to the higher number of charge carriers and to the lower activation energy: the more branched the polymers, the faster motion of charges due to a higher mobility of the polymeric chains. Interestingly, for temperatures above 75 °C the activation energies are almost half, and the conductivities are even closer to that of the pure ionic liquid. An inverse relationship between T_g and ionic conductivity can be observed: the ionic conductivity increases with a decrease of T_g and incremental amounts of PEGMEA, as it loosens the solid network and boosts the polymer motion inducing a suppression of T_g to lower temperatures. The amorphous phase of the solid polyionic electrolyte [36] and the introduction of PEGMEA with methoxyl chain end groups is therefore highly beneficial for ionic conductivity. The use of acrylate groups for polymerization, instead of methacrylate groups, also yields low T_g and thus high conductivity [37]. FESEM images acquired with InLens detector showed no solid phases, and the roughness evidenced by the image in Fig. 2 f is due only to the casting support (additional images are presented in the Supporting Information).

3.3. Wire-shaped all solid state supercapacitors

By scaling down the electrolyte volume for micro-devices, some specific requirements are compromised on a solid polymer electrolyte. The great challenge is to fabricate a conformal and uniform electrolyte coating with micrometers or sub-micrometers thickness, pinhole-free electrolyte layer with good mechanical stability, so that the short-circuit is avoided and a reasonable separation between negative and positive electrodes is maintained. Indeed, the solid-state conduction of

Table 2
Comparison of the glass transition temperature of the polyionic solid electrolytes presented in this work in comparison with those obtained by Fu et al. without electrolyte.

Fu et al. [23]		Our work				
co-polymer composition	*Glass transition temperature*	*co-polymer composition*	*Glass transition temperature*	*Ionic conductivity*	*Estimated limiting ionic conductivity*	*Activation energy up to 75°C*
	°C	40EMIMTFSI	°C	mS/cm	mS/cm at	kJ/mol
		40LiTFSI		at 25–125 °C	−273.15 °C	
	T_g		T_g	σ	σ_0	E_a
100PEGDA 0PEGMEA	−20	20PEGDA 0PEGMEA	−43.6	0.029–1.91	996	42.1
75PEGDA 25PEGMEA	−25	15PEGDA 5PEGMEA	−44.5	0.058–2.48	1396	41.3
50PEGDA 50PEGMEA	−31	10PEGDA 10PEGMEA	−45.4	0.088–3.26	1489	40.2
25PEGDA 75PEGMEA	−39	5PEGDA 15PEGMEA	−46.3	0.20–7.82	3100	40.1

ions becomes the minor problem when downscaling the thickness of the ion path: ionic conductivities higher than 10^{-3} mS cm^{-1} could be considered acceptable. More importantly, the electrolyte should maintain electronic insulation to avoid the self-discharge, therefore $\sigma_{electronic}$ should be lower than 10^{-7} mS cm^{-1} [38]. The most challenging goal for the use of solid electrolytes is surface wettability: while liquid electrolytes easily wet and penetrate highly porous structures, polymer films instead provide random contact points on the electrode surface. On non-planar substrates it is extremely hard to obtain a uniform, good coating of polymers by using conventional deposition methods such as chemical deposition (i.e. plasma polymerization) and physical deposition (i.e. solution-casting, doctor-blading, spin-coating). Achieving good interfacial interactions is even harder when very hydrophobic surfaces with high aspect ratios are employed, such as self-standing carbon nanotubes. We overcame these difficulties in covering the yCNT well simply by employing a blend with a viscosity between 30 and 90 Pa s and by placing in vacuum the electrodes immersed in the blend for 12 h prior to the UV polymerization.

In order to maximize the energy output of the wearable devices, asymmetric supercapacitors were designed so that the capacitance at the positive and negative electrodes was balanced. The understanding of the electrochemical stability window (ESW) of each electrode was therefore fundamental to design the appropriate volume of electrodes that determine the energy and power capabilities of the supercapacitors. The electrodes of yCNT and activated-yCNT, prepared as previously mentioned, were therefore placed in a homemade three electrode pouch cell with a titanium pseudo-reference electrode and a planar activated carbon coated-aluminum as counter electrode together with the most conductive solid electrolyte. The cell assembly is presented in Fig. 3 and as a picture in Fig. 4 a.

Cyclic voltammetries at 1 mV/s were carried out at the yarn electrodes to determine the anodic and cathodic potential limits at room temperature (22 °C). As explained for Fig. 1 e, the activated-yCNT massively loses ESW at positive potentials with respect to the open circuit potential (OCP), while, in the negative overpotential range, the capacitance increases. For these reasons, the data with the solid polyionic electrolyte of the yCNT are reported in both the negative and positive potential windows, while those for the activated-yCNT are shown only for the negative potential window (data in Fig. 4b).

As shown in Fig. 4 b, the highest coulombic efficiency was recorded at the potential of −0.6 V on the activated-yCNT (2.7 mF/cm) and +0.85 V on the yCNT (1.2 mF/cm). Such positive potential can be linked to the high oxidative activity due to the interaction between the –OH terminal groups of PEG-based polymer and the electrodes [39]. In contrast, the negative electrode does not at such low rates show the typical rectangular figure-of-merit due to the increased resistivity induced by the activation, as explained in the previous paragraphs. This current response also massively influenced the output of the asymmetric device which has been made by balancing the capacities of the negative electrode with the one at the positive terminal, in which the amount of the yCNT has been doubled to respect the charge balance and to maximize the energy output. Therefore, both symmetric and asymmetric cells were compared. In order to demonstrate the practical feasibility, the full solid-state cell (picture of Fig. 4c) was made with the following procedure: the electrodes were firstly gently coated with a thin solid polymer electrolyte layer, then the electrodes were twisted and more solid electrolyte was added prior to the pouch-sealing which prevented any moisture decreasing the performances. The all-solid-state wire device was cycled dynamically in order to immediately observe any variation in the voltammetry. As the data in Fig. 4 d show, for the asymmetric device the highest energy density of 1.3 μWh/cm has been recorded at a voltage of 2.3 V with a capacitance of 1.8 mF/cm and a fair coulombic efficiency of 99.7% (1 mV/s). The symmetric device, in contrast, provided 0.6 μWh/cm at 1.7 V with 1.4 mF/cm and 99.9% of efficiency. In Fig. 4 e, the rate capability test shows a steep increase in the capacitance for rates below 10 mV/s with coulombic efficiency still above 95%. The capacitance retention test was carried out at 1 mV/s for 1200 cycles. The devices both show good cycling stability, which is also a sign of good coulombic efficiency. Even though the specific capacity obtained is lower when compared to that of liquid electrolytes, the all-solid-state cells show a capacitance retention above 100% compared to the initial cycles, confirming the stable interfacial contact between the yCNT and the electrolyte even in such a challenging design (Fig. 4f). Float tests were carried out by placing the device at its maximum voltage for 24 h and recording a leakage current. At short times, the current is high, and it falls over time until it reaches a steady-state current which is equal to the current associated with the reactions of the faradaic contribution to the self-discharge [40]. After 24 h of charging, the leakage current was 8.3 a 30 μA/cm for the symmetric and asymmetric devices, respectively. The discharge profiles at OCP indicate that for both the devices the main self-discharge process is diffusion-controlled as evidenced by the potential vs time trend which is linear with respect to the square root of the

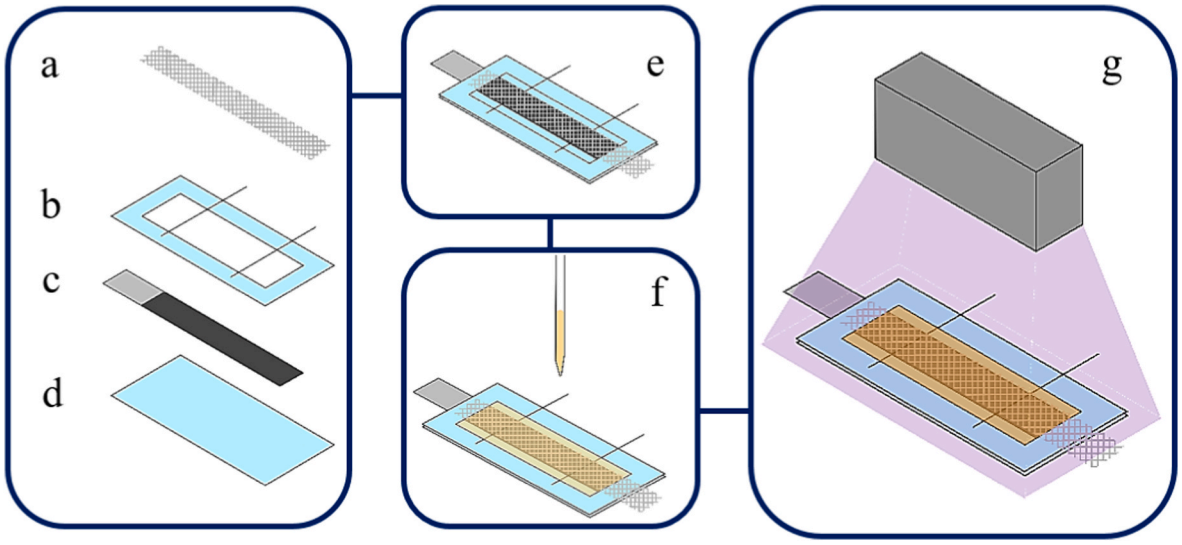

Fig. 3. Sketch of the assembly of the three electrodes cell: (a) titanium gauge as pseudo-reference electrode (b) yCNT and activated yCNT over the sealing tape, (c) activated carbon over aluminum current collector as counter electrode, (d) glass support. (e) Three-electrodes homemade cell, (f) filling of the cell with the electrolyte blend and (g) UV-curing under UV light of the electrolyte blend. (A colour version of this figure can be viewed online.)

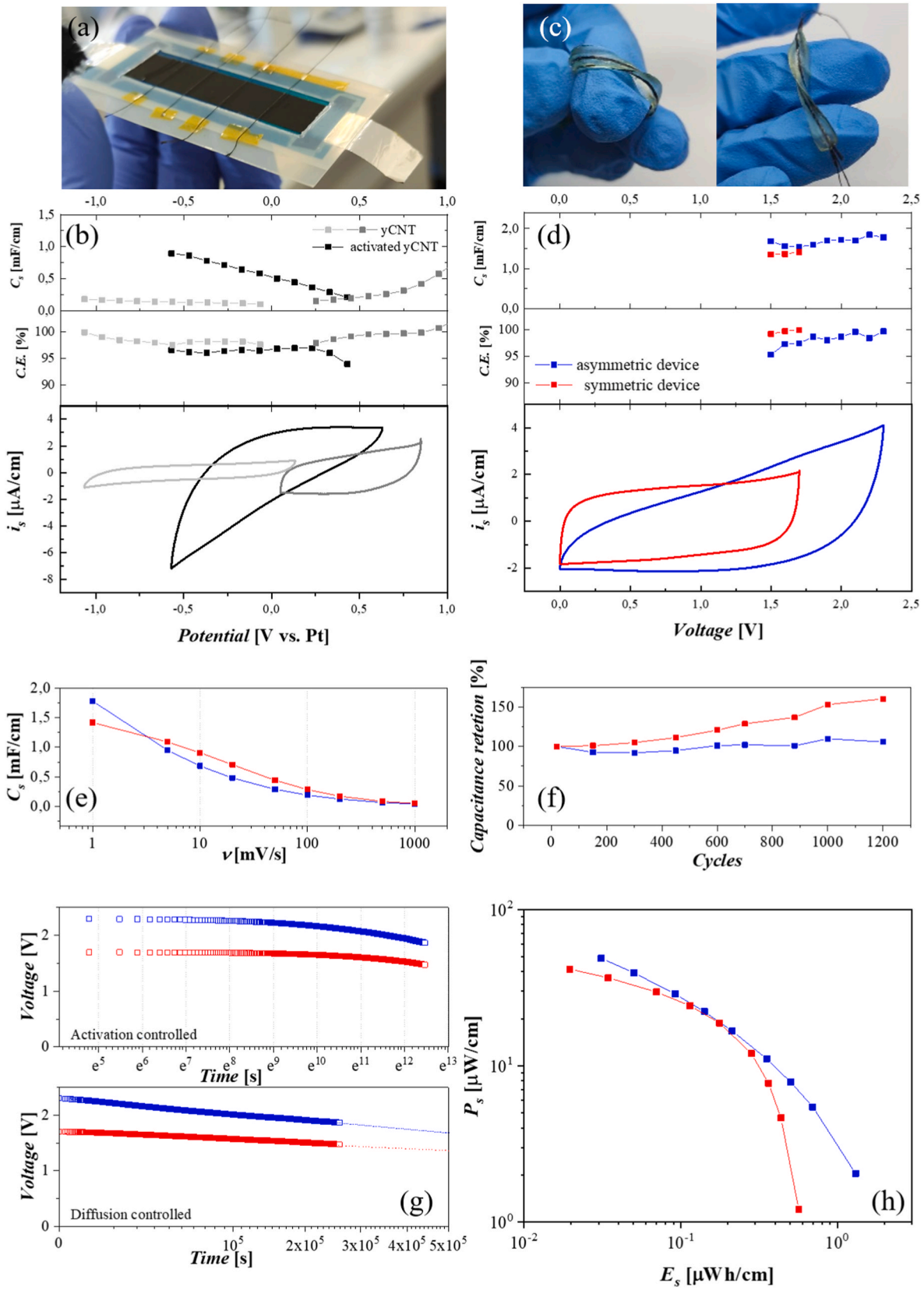

Fig. 4. Picture (a) and cyclic voltammetries (b) of the yCNT and activated yCNT in a three electrode configuration. Picture (c) and cyclic voltammetries (d) of the symmetric (red) and asymmetric (blue) devices. Plot of (e) rate capability, (f) capacitance retention, (g) self-discharge and (h) Ragone grid of the two devices. (A colour version of this figure can be viewed online.)

time (Fig. 4g) [40]. According to the potential decay, therefore, a fully-charged device at its maximum voltage is expected to fully self-discharge at 0 V in 74 h for the asymmetric configuration and in 150 h for the symmetric configuration.

In the literature, most of the *fiber*- and *wire*-shaped supercapacitors are assembled with gel electrolytes based on hydrogels of PAAM [41], CMC [42,43] or PVA and inorganic salts [44–50] or even with strong acids [51–59] and strong hydroxydes [60–62] with operative voltages between 0.8 and 1.8 V. To the best of our knowledge, only Naderi et al. reported an operative voltage window with 95% of coulombic efficiency at 2.0 V, employing a hydrogel of CMC with Na_2SO_4 [63] with a quite complex procedure to produce the negative (PEDOT:PSS–rGO on a carbon fiber) and positive electrodes (nanocomposite of MnO_2). Very recently, gel-based organic electrolytes [64] started to be employed also for wire-shaped supercapacitors, but still with a gel-texture and the presence of a solvent such as propylene carbonate [65]. As most of the research paper is based on hydrogels, to the best of our knowledge, this is the first evidence of a combination of a wire-shaped supercapacitor with a truly solid-state electrolyte avoiding the risks of leakage and drying and prepared with a very simple and scalable procedure to modulate the capacitance at the electrodes.

4. Conclusion

This research demonstrates and proves the possibility to design a true full solid state high-power device in the shape of a flexible wire storage element that can be easily integrated into smart textiles. The approach can be extended as a proof-of-concept to other energy device applications in which a high-aspect ratio of the materials is required together with no leakage of a high conductive electrolyte. The preparation method of the electrolytes points to the possibility of modulating their composition (solid salts, ionic liquid, proportion among polymeric precursors) for a specific purpose such as high conductivity, high flexibility, high alkaline metal concentration, high sustainability (no solvents nor chemical plants), etc. The possibility of using a tuneable full solid-state flexible high-power device opens a direct and efficient integration with harvesting systems and low energy loads. The shown devices were made either by using modified and unmodified CNT yarns and a blend of ionic liquid, Li salt and poly(ethylene glycol) acrylates. The most conductive mixture made it possible to obtain excellent performances of electrochemical stability and relevant power to energy densities by maintaining extreme flexibility even under high temperatures (125 °C). The results show the highest capacitance of 1.8 mF/cm, energy density of 1.3 μWh/cm and a capacitance retention higher than 100% over 1200 cycles with an asymmetric all solid-state wire-shaped device.

Data availability

Data will be made available on request.

CRediT authorship contribution statement

Mara Serrapede: Conceptualization, Formal analysis, Methodology, Investigation, Writing – original draft. **Francesco Seller:** Conceptualization, Data curation, Formal analysis, Methodology, Investigation, Writing – review & editing. **Pietro Zaccagnini:** Conceptualization, Formal analysis, Methodology, Investigation, Writing – review & editing. **Micaela Castellino:** Formal analysis, Methodology, Investigation, Writing – review & editing. **Ignazio Roppolo:** Formal analysis, Methodology, Investigation, Writing – review & editing. **Felice Catania:** Formal analysis, Investigation, Writing – review & editing. **Jennifer Tata:** Funding acquisition, Project administration. **Tiziano Serra:** Funding acquisition, Project administration. **Stefano Bianco:** Formal analysis, Methodology, Investigation, Writing – review & editing. **Andrea Lamberti:** Conceptualization, Methodology, Funding acquisition, Project administration, Supervision, Writing – original draft.

Declaration of competing interest

The authors declare that they have no known competing financial interests or personal relationships that could have appeared to influence the work reported in this paper.

Appendix A. Supplementary data

Supplementary data to this article can be found online at https://doi.org/10.1016/j.carbon.2023.118283.

References

[1] X. Wang, K. Jiang, G. Shen, Flexible fiber energy storage and integrated devices: recent progress and perspectives, Mater. Today 18 (2015) 265–272.
[2] A. Lamberti, A. Gigot, S. Bianco, M. Fontana, M. Castellino, E. Tresso, C.F. Pirri, Self-assembly of graphene aerogel on copper wire for wearable fiber-shaped supercapacitors, Carbon 105 (2016) 649–654.
[3] M. Parmeggiani, S. Stassi, M. Fontana, S. Bianco, F. Catania, L. Scaltrito, A. Lamberti, Laser-induced graphenization of textile yarn for wearable electronics application, Smart Mater. Struct. 30 (2021), 105007.
[4] H.-R. Yao, Y.-X. Yin, Y.-G. Guo, Size effects in lithium ion batteries, Chin. Phys. B 25 (2016), 018203.
[5] L. Dong, C. Xu, Y. Li, Z.-H. Huang, F. Kang, Q.-H. Yang, X. Zhao, Flexible electrodes and supercapacitors for wearable energy storage: a review by category, Journal of Materials Chemistry A 4 (2016) 4659–4685.
[6] J. Muldoon, C.B. Bucur, N. Boaretto, T. Gregory, V. di Noto, Polymers: opening doors to future batteries, Polym. Rev. 55 (2015) 208–246.
[7] V. Dinoto, E. Negro, S. Lavina, M. Vittadello, 6 - hybrid inorganic–organic polymer electrolytes, in: C. Sequeira, D. Santos (Eds.), Polymer Electrolytes, Woodhead Publishing, 2010, pp. 219–277.
[8] N. Boaretto, L. Meabe, M. Martinez-Ibañez, M. Armand, H. Zhang, Review—polymer electrolytes for rechargeable batteries: from nanocomposite to nanohybrid, J. Electrochem. Soc. 167 (2020), 070524.
[9] W. Zhu, X. Zhang, Y. Yin, Y. Qin, J. Zhang, Q. Wang, In-situ electrochemical activation of carbon fiber paper for the highly efficient electroreduction of concentrated nitric acid, Electrochim. Acta 291 (2018) 328–334.
[10] Y. Yi, G. Weinberg, M. Prenzel, M. Greiner, S. Heumann, S. Becker, R. Schlögl, Electrochemical corrosion of a glassy carbon electrode, Catal. Today 295 (2017) 32–40.
[11] D.E. Fenton, J.M. Parker, P.V. Wright, Complexes of alkali metal ions with poly (ethylene oxide), Polymer 14 (1973) 589.
[12] Fast Ion Transport in Solids: Electrodes, and Electrolytes.
[13] M.B. Armand, P.G. Bruce, M. Forsyth, B. Scrosati, W. Wieczorek, Polymer Electrolytes, Energy Materials, 2011, pp. 1–31.
[14] J.W. Fergus, Ceramic and polymeric solid electrolytes for lithium-ion batteries, J. Power Sources 195 (2010) 4554–4569.
[15] S. Cheng, D.M. Smith, Q. Pan, S. Wang, C.Y. Li, Anisotropic ion transport in nanostructured solid polymer electrolytes, RSC Adv. 5 (2015) 48793–48810.
[16] B. Sun, D. Rehnlund, M.J. Lacey, D. Brandell, Electrodeposition of thin poly (propylene glycol) acrylate electrolytes on 3D-nanopillar electrodes, Electrochim. Acta 137 (2014) 320–327.
[17] M. Echeverri, C. Hamad, T. Kyu, Highly conductive, completely amorphous polymer electrolyte membranes fabricated through photo-polymerization of poly (ethylene glycol diacrylate) in mixtures of solid plasticizer and lithium salt, Solid State Ionics 254 (2014) 92–100.
[18] Y. Cui, J. Zhang, P. Wang, X. Zhang, J. Zheng, Q. Sun, J. Feng, Y. Zhu, Improved performance using a plasticized polymer electrolyte for quasi-solid state dye-sensitized solar cells, Electrochim. Acta 74 (2012) 194–200.
[19] Q. Zhou, K. Fitzgerald, P.D. Boyle, W.A. Henderson, Phase behavior and crystalline phases of ionic liquid-lithium salt mixtures with 1-Alkyl-3-methylimidazolium salts, Chem. Mater. 22 (2010) 1203–1208.
[20] B. Sun, I.Y. Liao, S. Tan, T. Bowden, D. Brandell, Solid polymer electrolyte coating from a bifunctional monomer for three-dimensional microbattery applications, J. Power Sources 238 (2013) 435–441.
[21] B. Kaczmarczyk, B. Morejko-Buż, A. Stolarzewicz, Investigation of infrared calibration methods for application to the study of methyl methacrylate polymerization, Fresen. J. Anal. Chem. 370 (2001) 899–903.
[22] H.A. Albehaijan, C.R. Piedrahita, J. Cao, M. Soliman, S. Mitra, T. Kyu, Mechanoelectrical transduction of polymer electrolyte membranes: effect of branched networks, ACS Appl. Mater. Interfaces 12 (2020) 7518–7528.
[23] G. Fu, T. Kyu, Effect of side-chain branching on enhancement of ionic conductivity and capacity retention of a solid copolymer electrolyte membrane, Langmuir 33 (2017) 13973–13981.
[24] A. Achour, S. Vizireanu, G. Dinescu, L. Le Brizoual, M.A. Djouadi, M. Boujtita, Electrochemical anodic oxidation of nitrogen doped carbon nanowall films: X-ray photoelectron and Micro-Raman spectroscopy study, Appl. Surf. Sci. 273 (2013) 49–57.
[25] N.G. Shang, F.C.K. Au, X.M. Meng, C.S. Lee, I. Bello, S.T. Lee, Uniform carbon nanoflake films and their field emissions, Chem. Phys. Lett. 358 (2002) 187–191.

[26] A. Eckmann, A. Felten, A. Mishchenko, L. Britnell, R. Krupke, K.S. Novoselov, C. Casiraghi, Probing the nature of defects in graphene by Raman spectroscopy, Nano Lett. 12 (2012) 3925–3930.
[27] M. Smith, L. Scudiero, J. Espinal, J.-S. McEwen, M. Garcia-Perez, Improving the deconvolution and interpretation of XPS spectra from chars by ab initio calculations, Carbon 110 (2016) 155–171.
[28] N. Badi, A.M. Theodore, S.A. Alghamdi, H.A. Al-Aoh, A. Lakhouit, P.K. Singh, M. N. Norrrahim, G. Nath, The Impact of Polymer Electrolyte Properties on Lithium-Ion Batteries, 2022. Polymers.
[29] K. Karuppasamy, H.W. Rhee, P.A. Reddy, D. Gupta, L. Mitu, A.R. Polu, X. Sahaya Shajan, Ionic liquid incorporated nanocomposite polymer electrolytes for rechargeable lithium ion battery: a way to achieve improved electrochemical and interfacial properties, J. Ind. Eng. Chem. 40 (2016) 168–176.
[30] G. González, D. Baruffaldi, C. Martinengo, A. Angelini, A. Chiappone, I. Roppolo, C. F. Pirri, F. Frascella, Materials Testing for the Development of Biocompatible Devices through Vat-Polymerization 3D Printing, 2020. Nanomaterials.
[31] B. Tosetto, M. Gastaldi, G. Renno, C.F. Pirri, C. Barolo, A. Fin, I. Roppolo, Colorimetric 3D printable base-detectors exploiting halocromic core-substituted naphthalenediimides, Polym. Chem. 14 (2023) 1213–1223.
[32] S. Stassi, E. Fantino, R. Calmo, A. Chiappone, M. Gillono, D. Scaiola, C.F. Pirri, C. Ricciardi, A. Chiadò, I. Roppolo, Polymeric 3D printed functional microcantilevers for biosensing applications, ACS Appl. Mater. Interfaces 9 (2017) 19193–19201.
[33] R.A. Voronkov, N. Medvedev, A.E. Volkov, Superionic states formation in group III oxides irradiated with ultrafast lasers, Sci. Rep. 12 (2022) 5659.
[34] Y. Okada, M. Ikeda, M. Aniya, Non-Arrhenius ionic conductivity in solid electrolytes: a theoretical model and its relation with the bonding nature, Solid State Ionics 281 (2015) 43–48.
[35] M. Ikeda, M. Aniya, Bond Strength—Coordination Number Fluctuation Model of Viscosity: an Alternative Model for the Vogel-Fulcher-Tammann Equation and an Application to Bulk Metallic Glass Forming Liquids, 2010, pp. 5246–5262. Materials.
[36] P. Johansson, First principles modelling of amorphous polymer electrolytes: Li+–PEO, Li+–PEI, and Li+–PES complexes, Polymer 42 (2001) 4367–4373.
[37] N. Paranjape, P.C. Mandadapu, G. Wu, H. Lin, Highly-branched cross-linked poly (ethylene oxide) with enhanced ionic conductivity, Polymer 111 (2017) 1–8.
[38] J. Mindemark, M.J. Lacey, T. Bowden, D. Brandell, Beyond PEO—alternative host materials for Li+-conducting solid polymer electrolytes, Prog. Polym. Sci. 81 (2018) 114–143.
[39] H. Zhang, C. Liu, L. Zheng, F. Xu, W. Feng, H. Li, X. Huang, M. Armand, J. Nie, Z. Zhou, Lithium bis(fluorosulfonyl)imide/poly(ethylene oxide) polymer electrolyte, Electrochim. Acta 133 (2014) 529–538.
[40] H.A. Andreas, Self-discharge in electrochemical capacitors: a perspective article, J. Electrochem. Soc. 162 (2015) A5047–A5053.
[41] F.-L. Yi, F.-C. Meng, Y.-Q. Li, P. Huang, N. Hu, K. Liao, S.-Y. Fu, Highly stretchable CNT Fiber/PAAm hydrogel composite simultaneously serving as strain sensor and supercapacitor, Compos. B Eng. 198 (2020), 108246.
[42] Z. Yang, W. Zhao, Y. Niu, Y. Zhang, L. Wang, W. Zhang, X. Xiang, Q. Li, Direct spinning of high-performance graphene fiber supercapacitor with a three-ply core-sheath structure, Carbon 132 (2018) 241–248.
[43] J.T. Carvalho, I. Cunha, J. Coelho, E. Fortunato, R. Martins, L. Pereira, Carbon-yarn-based supercapacitors with in situ regenerated cellulose hydrogel for sustainable wearable electronics, ACS Appl. Energy Mater. 5 (2022) 11987–11996.
[44] M. Serrapede, A. Rafique, M. Fontana, A. Zine, P. Rivolo, S. Bianco, L. Chetibi, E. Tresso, A. Lamberti, Fiber-shaped asymmetric supercapacitor exploiting rGO/Fe2O3 aerogel and electrodeposited MnOx nanosheets on carbon fibers, Carbon 144 (2019) 91–100.
[45] W. Gong, B. Fugetsu, Z. Wang, T. Ueki, I. Sakata, H. Ogata, F. Han, M. Li, L. Su, X. Zhang, M. Terrones, M. Endo, Thicker carbon-nanotube/manganese-oxide hybridized nanostructures as electrodes for the creation of fiber-shaped high-energy-density supercapacitors, Carbon 154 (2019) 169–177.
[46] X. Wang, Z. Zhou, Z. Sun, J. Hah, Y. Yao, K.-S. Moon, J. Di, Q. Li, C.-p. Wong, Atomic modulation of 3D conductive frameworks boost performance of MnO2 for coaxial fiber-shaped supercapacitors, Nano-Micro Lett. 13 (2020) 4.
[47] C. Yu, Y. Gong, R. Chen, M. Zhang, J. Zhou, J. An, F. Lv, S. Guo, G. Sun, A solid-state fibriform supercapacitor boosted by host–guest hybridization between the carbon nanotube scaffold and MXene nanosheets, Small 14 (2018), 1801203.
[48] A. Rafique, A. Massa, M. Fontana, S. Bianco, A. Chiodoni, C.F. Pirri, S. Hernández, A. Lamberti, Highly uniform anodically deposited film of MnO2 nanoflakes on carbon fibers for flexible and wearable fiber-shaped supercapacitors, ACS Appl. Mater. Interfaces 9 (2017) 28386–28393.
[49] A. Pedico, A. Lamberti, A. Gigot, M. Fontana, F. Bella, P. Rivolo, M. Cocuzza, C. F. Pirri, High-performing and stable wearable supercapacitor exploiting rGO aerogel decorated with copper and molybdenum sulfides on carbon fibers, ACS Appl. Energy Mater. 1 (2018) 4440–4447.
[50] A. Rafique, S. Bianco, M. Fontana, C.F. Pirri, A. Lamberti, Flexible wire-based electrodes exploiting carbon/ZnO nanocomposite for wearable supercapacitors, Ionics 23 (2017) 1839–1847.
[51] M. Tang, Y. Wu, J. Yang, Y. Xue, Hierarchical core-shell fibers of graphene fiber/radially-aligned molybdenum disulfide nanosheet arrays for highly efficient energy storage, J. Alloys Compd. 828 (2020), 153622.
[52] C. Shen, Y. Xie, B. Zhu, M. Sanghadasa, Y. Tang, L. Lin, Wearable woven supercapacitor fabrics with high energy density and load-bearing capability, Sci. Rep. 7 (2017), 14324.
[53] J. Kim, J. Yin, X. Xuan, J.Y. Park, A flexible cable-shaped supercapacitor based on carbon fibers coated with graphene flakes for wearable electronic applications, Micro and Nano Systems Letters 7 (2019) 4.
[54] L. Chen, D. Li, L. Chen, P. Si, J. Feng, L. Zhang, Y. Li, J. Lou, L. Ci, Core-shell structured carbon nanofibers yarn@polypyrrole@graphene for high performance all-solid-state fiber supercapacitors, Carbon 138 (2018) 264–270.
[55] W. Ma, S. Chen, S. Yang, W. Chen, W. Weng, Y. Cheng, M. Zhu, Flexible all-solid-state asymmetric supercapacitor based on transition metal oxide nanorods/reduced graphene oxide hybrid fibers with high energy density, Carbon 113 (2017) 151–158.
[56] C. Bai, Y. Wang, Z. Fan, L. Yan, H. Jiao, One-step preparation of gel-electrolyte-friendly fiber-shaped aerogel current collector for solid-state fiber-shaped supercapacitors with large capacity, J. Power Sources 521 (2022), 230971.
[57] S. Yu, B. Patil, H. Ahn, Flexible, fiber-shaped supercapacitors with roll-type assembly, J. Ind. Eng. Chem. 71 (2019) 220–227.
[58] S. Pan, J. Deng, G. Guan, Y. Zhang, P. Chen, J. Ren, H. Peng, A redox-active gel electrolyte for fiber-shaped supercapacitor with high area specific capacitance, J. Mater. Chem. A 3 (2015) 6286–6290.
[59] X. Li, D. Liu, X. Yin, C. Zhang, P. Cheng, H. Guo, W. Song, J. Wang, Hydrated ruthenium dioxides @ graphene based fiber supercapacitor for wearable electronics, J. Power Sources 440 (2019), 227143.
[60] J. Sun, P. Man, Q. Zhang, B. He, Z. Zhou, C. Li, X. Wang, J. Guo, J. Zhao, L. Xie, Q. Li, J. Sun, G. Hong, Y. Yao, Hierarchically-structured Co3O4 nanowire arrays grown on carbon nanotube fibers as novel cathodes for high-performance wearable fiber-shaped asymmetric supercapacitors, Appl. Surf. Sci. 447 (2018) 795–801.
[61] R. Zhang, C. Chen, H. Yu, S. Cai, Y. Xu, Y. Yang, H. Chang, All-solid-state wire-shaped asymmetric supercapacitor based on binder-free CuO nanowires on copper wire and PPy on carbon fiber electrodes, J. Electroanal. Chem. 893 (2021), 115323.
[62] J. Zhang, P.S. Shewale, K.-S. Yun, Fiber-Shaped Supercapacitors Fabricated Using Hierarchical Nanostructures of NiCo2O4 Nanoneedles and MnO2 Nanoflakes on Roughened Ni Wire, 2019. Energies.
[63] L. Naderi, S. Shahrokhian, F. Soavi, Fabrication of a 2.8 V high-performance aqueous flexible fiber-shaped asymmetric micro-supercapacitor based on MnO2/PEDOT:PSS-reduced graphene oxide nanocomposite grown on carbon fiber electrode, J. Mater. Chem. A 8 (2020) 19588–19602.
[64] M. Shi, C. Yang, X. Song, J. Liu, L. Zhao, P. Zhang, L. Gao, Recoverable wire-shaped supercapacitors with ultrahigh volumetric energy density for multifunctional portable and wearable electronics, ACS Appl. Mater. Interfaces 9 (2017) 17051–17059.
[65] C. Choi, J.W. Park, K.J. Kim, D.W. Lee, M.J. de Andrade, S.H. Kim, S. Gambhir, G. M. Spinks, R.H. Baughman, S.J. Kim, Weavable asymmetric carbon nanotube yarn supercapacitor for electronic textiles, RSC Adv. 8 (2018) 13112–13120.